Journal of
Marine Science and Engineering

MDPI

Article

Analysis of Horizontal Cylinder Load under Different Conditions in Regards to Waves and Flows

Xiaoguo Zhou [1,*], Qingdian Jiang [1], Kai Wang [2] and Shuqi Wang [1]

[1] School of Naval Architecture and Ocean Engineering, Jiangsu University of Science and Technology, Zhenjiang 212100, China
[2] Wuhan Second Ship Design & Research Institute, Wuhan 430064, China
* Correspondence: zhouxg@just.edu.cn; Tel.:+86-138-5298-1438

Abstract: A numerical simulation based on the CFD method is used to study the interaction between a horizontal cylinder and wave flow. Firstly, a two-dimensional numerical calculation model of both a fixed and a rigid moving cylinder, with a free surface under varying wave flow conditions, is created. In the established model, the loads on the horizontal cylinder under different submergence depths, flow velocities, cylinder sizes, wave periods, and *k* values (spring stiffness) are analyzed and calculated. The results show that, when the cylinder is close to the free surface, its hydrodynamic load under wave flow conditions is more sensitive to changes in submergence depth, which essentially affects wave reflection and blockage. At different flow velocities, *k* values, cylinder radii, and arm lengths, the main frequency of the Fourier transform of the cylinder motion curve remains unchanged; however, the main frequency does change with the wave period and submergence depth. The efficiency of rotary cylindrical energy harvesting is influenced by various factors, among which an initial increase and then decrease are observed with a gradually increasing *k* value, arm length, period, and radius, in addition to an observed decrease with increasing flow velocity.

Keywords: horizontal cylinder; free surface; load analysis; rigid moving cylinder; hydrodynamic load

Citation: Zhou, X.; Jiang, Q.; Wang, K.; Wang, S. Analysis of Horizontal Cylinder Load under Different Conditions in Regards to Waves and Flows. *J. Mar. Sci. Eng.* **2024**, *12*, 1101. https://doi.org/10.3390/jmse12071101

Academic Editor: Marco Petti

Received: 26 May 2024
Revised: 23 June 2024
Accepted: 24 June 2024
Published: 28 June 2024

1. Introduction

The vast ocean contains abundant marine biological and mineral resources. In the equipment employed for developing such resources, a horizontal cylinder is a commonly used structure, which is often affected by the combined effects of ocean currents and waves in practical applications, resulting in adverse effects. In new types of ocean current energy, vortex-induced vibration can also be used for power generation. The study of the force and motion of cylindrical structures under wave current conditions is of great significance for the design and safety of ocean structures and further research on power generation devices.

Reichl [1,2] conducted a numerical simulation study on the vortex field around a cylinder, utilizing different submergence depths near the free surface under the action of flow. The results showed that the vortex field around the cylinder changed significantly with the change in submergence depth, and the smaller the submergence depth, the more asymmetric the vortex field. In addition, the influence of changes in the Froude number on the free surface and vortex field was also studied. Wu and Young [3] conducted numerical simulation research on the oscillatory motion of a horizontal cylinder in a stationary fluid; they presented the changes in the vortex field during cylinder motion, comparing and verifying the simulated force results with previously obtained results. This study focuses on the validation of numerical methods; the analysis of the fluid field characteristics around the cylinder is not extensively discussed, and the strong nonlinear phenomena in the selected operating conditions are not obvious. In the study of horizontal cylinders under differing wave current conditions, Bozkaya [4] used a self-developed finite volume method program to numerically simulate the vortex field around a vibrating cylinder in the flow. The study

mainly focused on the influence of two variables—the cylinder's vibration frequency and submergence depth—on the vortex field around the cylinder.

Xiao [5] conducted numerical simulations to investigate the interaction between solitary waves and horizontal cylinders. In this study, the factor of flow was considered, and the differences and similarities in the vortex field around the cylinder under the action of solitary waves were compared and analyzed under the following conditions: forward flow, no flow, and reverse flow. In addition, the influence of flow on the force of the cylinder was analyzed by comparing its force values under three different conditions. The research results indicate that the combined force of waves and currents is not equal to the superposition of both wave and current forces, while the influence of current on the horizontal force is particularly significant.

Bai [6] conducted a numerical simulation study on the interaction between regular waves and a horizontal cylinder, comparing the motion laws of the vortex field around the cylinder under both downstream and upstream conditions. The results showed that the wave and current jointly act as the vortex field, while the vortex leakage frequency is controlled by the frequency of the waves; that is, vortex shedding occurs in each wave cycle, which is different from the conventional cylinder flow problem, where vortex shedding only occurs after it matures.

Gu et al. [7] used a two-dimensional numerical simulation method to simulate a cylinder with springs installed in a power generation device. The water depth varied from 0.1 m to 0.5 m, and the energy conversion rate was studied at different submergence depths. The results showed that the free surface had a significant impact on the vortex-induced vibration response, wherein a decrease in submergence depth from 0.5 m to 0.1 m gradually suppressed the amplitude of vortex-induced vibration, leading to a decrease in the energy conversion rate.

Zhao et al. [8] used the dimensionless Rortex/Liutex vortex identification method to numerically simulate an infinitely long cylinder with a free surface, where Fr = 0.3 and Re = 4.2 $\times$ 104. The results showed that in the wake region near the free surface, the originally alternating shedding vortex street structure was strongly suppressed.

Wang et al. [9] proposed an upright flow-induced vibration energy harvesting system and designed relevant experiments. The experimental data showed that the optimal layout form for comparing the energy harvesting efficiency of cylinders under different spacing uses 2D spacing.

Wang et al. [10] used the time-domain finite element method to solve the second-order interaction problem between wave current and truncated double cylinders, calculating the wave and hydrodynamic forces of the double cylinders under the combined action of wave current. The results showed that the amplitude of the first-order horizontal and vertical forces on the cylinder increased with the increase in the Froude number.

Zhang et al. [11] used the fourth-order exact finite volume approach to simulate the interaction between solitary waves, uniform flows, and a horizontal cylinder near a free surface. The accuracy of the solution method was verified through experimental data of flow velocity under the interaction of solitary waves and flows. The results showed that under the interaction of waves and flows, there was a significant correlation between the vertical force on the cylinder and the flow velocity.

Lin et al. [12] used local and global empirical parameters and examined the influence of retaining nonlinear acceleration terms on the Morison equation. The results showed that the fitting effect was related to the position of the cylinder cross-section and had little effect on the lower section of the cylinder; the actual force could also be well-fitted to the upper section of the cylinder. After correcting the Morison equation, the prediction was more in line with the actual value.

Through a large number of wave current interaction experiments, Yang et al. [13] studied its influence on wave height and water velocity. The experimental results showed that, when solitary waves propagate with the flow, the flow velocity near the static water level is equal to the linear superposition of a single wave and single flow velocities.

Zang et al. [14] experimentally studied the hydrodynamic response of a vertical cylinder under wave action and flow wave composite action under finite water depth conditions. The experiment found that the multi-frequency response of the cylinder in the transverse flow direction is related to the natural frequency of the cylinder and the frequency of the wave, while the displacement of the cylinder mainly depends on the ratio of the natural frequency to the wave frequency, under wave action.

Xin et al. [15] proposed a method and verified its accuracy through numerical implementation, studying the coupling effect of waves on the hydrodynamic load of a cylinder near a free surface. The results showed that changes in submergence depth and the direction between waves and flow velocity play an important role in the cylinder's load.

Huo et al. [16] used OpenFOAM and numerical methods to study the hydrodynamic response under the combined action of waves and currents. A high-precision wave flow was generated using a buoyancy-corrected k-omega SST turbulence model; the relationship between shock pressure, relative wave height, and wave velocity was analyzed.

Ning et al. [17] established a two-dimensional nonlinear numerical wave tank based on the time-domain high-order boundary element method, using a four-point method to decompose the high bound and free harmonics propagating upstream and downstream along obstacles. The second-order analysis of the experimental results indicates that the resonance characteristics are related to the ratio of the diameter of the cylinder to the wavelength of its second bound mode.

Saincher et al. [18] analyzed the interaction between nonlinear waves and currents on ships and their effects on cylindrical hydrodynamic loads. Experiments have shown that wave and local action current loads can be linearly superimposed on structures and are unaffected by wave characteristics and resistance velocity.

Zhou et al. [19] established a numerical model of wave flow based on the CFD method and verified its accuracy with experimental data. By studying the hydrodynamic characteristics of a horizontal cylinder under different spring stiffness conditions, the results showed that with the increase in k value, the vibration amplitude of the cylinder first increased and then decreased. When the vibration amplitude reached its peak, the vibration frequency was consistent with the wave frequency, resulting in resonance.

Belloli et al. [20] compared the characteristics of vortex-excited vibration and subcritical vibration in the critical flow state. Manish A. [21] established a dual-degree-of-freedom model, and experimental results showed that the model could capture the jump in lateral flow response when a cylinder was freely moving along the crossflow direction in medium and low quality ratio cases; for high quality ratio, the response was not affected by the free movement along the flow direction, and it was found that the cause of the lateral vibration jump in the dual-degree-of-freedom system was the additional damping in the flow direction.

Sirohi [22] installed a D-shaped hemispherical truncated cone at the lower end of a PZT piezoelectric cantilever beam and experimentally measured the electrical energy generated by the prototype device, which was 325 mm long, in the wind speed range and demonstrated the feasibility of collecting wind energy using the device; the power output increased rapidly with the increase in wind speed. Abdelkefi [23] studied the wind-induced galloping characteristics by means of a double-cantilever piezoelectric model, verified the galloping starting speed of the test data through linear analysis, and studied the effects of load resistance and wind speed on the power harvest, transverse displacement, and voltage output level. The results show that the maximum power level and minimum lateral displacement can be obtained when the load resistance is changed at a certain wind speed.

Overall, in the study of the above flow field, the main focus is on completely submerged cylinders, with more consideration being given to the vertical motion of the cylinders. Among them, the consideration of rotating cylinders is currently insufficient, and there is little research regarding the strong interaction between free surfaces and cylinders. Therefore, this paper focuses on the characteristics of the flow field around a rotating cylinder near a free surface. By comparing the force conditions of a fixed and a rotating

cylinder, the load characteristics of the cylinder under the combined action of waves and currents are studied.

2. Model Establishment

2.1. Fluid Control Equation

The model uses the finite volume method to solve the Reynolds averaged N-S equation; the control equation is as follows:

$$\frac{\partial v_i}{\partial x_i} = 0 \tag{1}$$

$$\frac{\partial \rho v_i}{\partial t} + \frac{\partial \rho v_i v_j}{\partial x_j} = -\frac{\partial p}{\partial x_i} + \mu \frac{\partial}{\partial xj}\left(\frac{\partial v_i}{\partial x_j} + \frac{\partial v_j}{\partial x_i}\right) + \rho g \tag{2}$$

where v_i and v_j are the component of fluid particle velocity in the i and j directions, respectively; t is time; p is the fluid pressure; ρ is the fluid density; μ is the viscosity coefficient of the fluid; and g is the gravitational acceleration.

The free surface of the numerical model using the VOF method is captured, and the volume fraction of each calculation unit is represented as follows [9], 0 is air, 1 is water, and 0 to 1 indicates the mixed state of water and air, also known as the free surface:

$$\alpha = \begin{cases} 0 & air \\ 0 \sim 1 & free\ surface \\ 1 & water \end{cases} \tag{3}$$

The density and viscosity coefficient of the mixed fluid can be obtained using the following formula:

$$\rho = \alpha\rho_w + (1-\alpha)\rho_a \tag{4}$$

$$\mu = \alpha\mu_w + (1-\alpha)\mu_a \tag{5}$$

where the subscript w represents the liquid phase and a represents the gas phase.

A reduced velocity is used to reflect the relationship between amplitude and flow velocity, expressed as follows:

$$U_r = \frac{U}{Df_n} \tag{6}$$

where U is the inflow velocity, f_n is the natural frequency of the cylinder, and D is the diameter of the cylinder.

2.2. Establishing a Computational Model

A cylindrical solution domain containing background and overlapping grids is established, as shown in Figures 1 and 2. The diameter, D, of the cylinder in the solution domain is 0.1 m; the cylinder is defined as a wall with a water depth, d, of 1 m; the flow velocity is 0.25 m/s; the total number of grids is 228,600; and the solution time step is 0.002 s. A total of 10 boundary layers were set around the cylinder, and multiple refinement is carried out near the free surface on the grid division. The left side is the velocity inlet, and the velocity is given as required; the right and top sides are pressure outlets and yield relative pressures, while the bottom side and cylinder surface are the wall boundary. To simulate cylindrical motion, the cylinder is set as a rigid body and is given a spring stiffness and damping ratio. According to Ref. [24], the turbulence model is selected as the RNG turbulence model. There are three commonly used numerical discretization methods: the finite element method, the finite difference method, and the finite volume method. The numerical model adopted in this paper is the finite volume method, and the model is a two-dimensional model with two degrees of freedom, the horizontal x direction and the vertical z direction. The model is simplified, and no other deformation is taken into account [25].

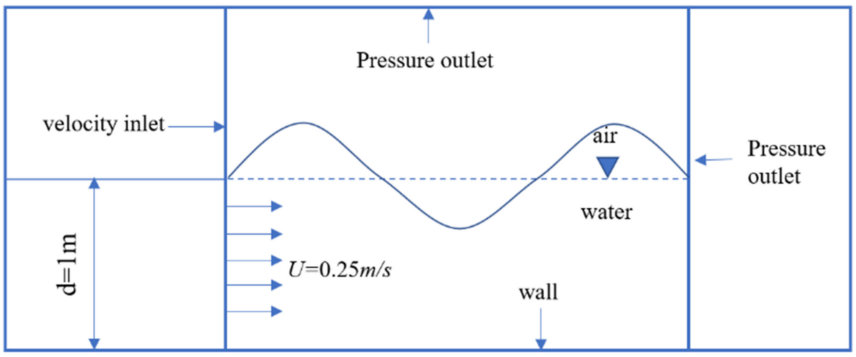

Figure 1. Computational domain model.

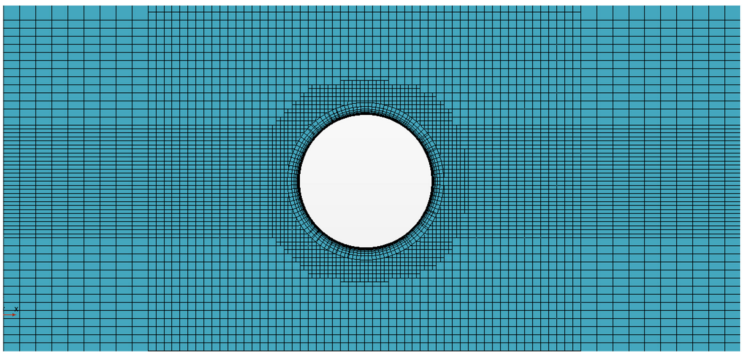

Figure 2. Grid model.

On the basis of the fixed model, a refined region is incorporated into the rotating motion model to ensure that the cylinder's movement remains within this refined region. Additional parameters, such as the moment of inertia and the center of gravity, are included in the cylinder parameters, while maintaining an unchanged damping ratio equal to 0.02. The virtual rod fixed point is positioned horizontally downstream from the cylinder and connected to it through a volumetric coupling function. The virtual rod is rigid, allowing the cylinder to rotate around this fixed point. Furthermore, an adjustable rotation torque for the cylinder has been integrated into the model.

2.3. Grid Convergence Analysis

According to the relevant literature on numerical calculations, the grid size affects the accuracy of the numerical calculations, especially in the direction of wave propagation and wave height. Therefore, while ensuring computational accuracy and reducing the number of grids and the simulation time, this section starts with a convergence verification of the grid in the wave region, with the aim of obtaining a more accurate wave simulation with the least number of grids.

In this section, three types of meshing are used for the numerical wave flume, wave simulation is carried out under the same operating conditions, and finally, the lowest amount of mesh and an increased accuracy are obtained by comparing the simulated values. Due to the complexity of fluid changes, a more precise grid is required to capture the changes in the flow field. Therefore, this paper has set up five layers of grids around the wave situation; the closer the grid is to the free surface, the denser it is. Table 1 shows the specific dimensions of three types of grid refinement. This simulation is conducted under wave conditions of $S = 0$ and $A = 0.05$ m, with a unified time step of 0.002 s. The altimeter settings are as follows: altimeter 1 is located at 1.65 L in the working area, and altimeter 2 is located at 1.85 L.

Table 1. Grid parameters.

Grid	Number of Grids within the Wavelength Range	Number of Grids within the Wave Height Range	Total Number of Two-Dimensional Grids
1	80	15	1.82×10^5
2	100	20	2.28×10^5
3	120	25	2.72×10^5

Figure 3 shows the wave height–time history curves of two different wave altimeters under three different grids within a time period of 18 s~25 s. By comparing the data in the figure, it can be concluded that the waves under the three grids are consistent in terms of wave height and period. In summary, the results of Grid 3 and Grid 2 are consistent, while there are some differences between the results of Grid 1 and Grid 2, i.e., Grids 2 and 3 meet the convergence requirements. Therefore, considering computational accuracy and cost, Grid 2 is chosen as the final computational grid.

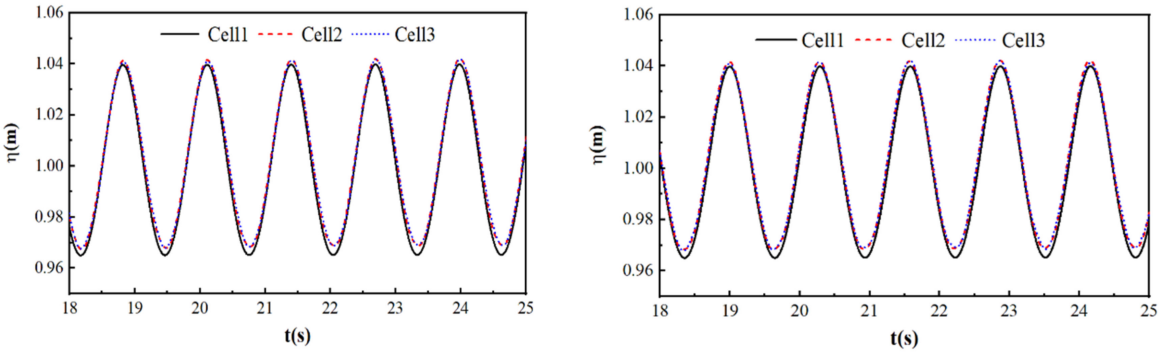

(**a**) Wave altimeter 1 (**b**) Wave altimeter 2

Figure 3. Comparison of wave height–time history curves with different grid numbers.

2.4. Numerical Verification of Wave and Current Forces

Referring to the physical experimental values of Bai et al. [6], the wave current force acting on a semi-submerged horizontal cylinder was verified. As shown in Figure 4, a horizontal cylinder with a diameter of D = 0.06 m, a depth of d = 1.6 m, a flow velocity of c = 0.2 m/s, an incident wave period of T = 0.7 s, and a wave height of H = 0.03 m was partially submerged in water.

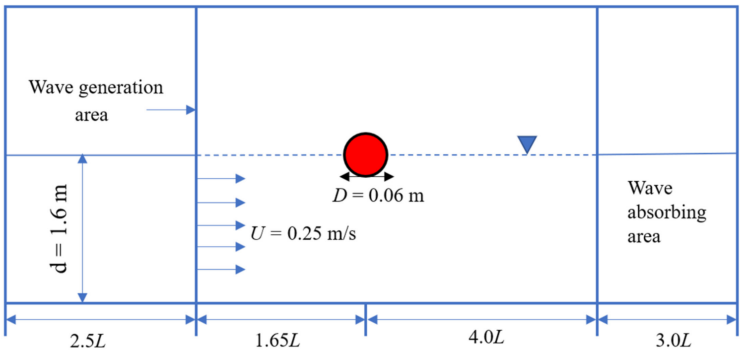

Figure 4. Schematic diagram of numerical water tank simulation.

The dimensionless processing of all force data in this paper is based on the buoyancy experienced by a horizontal cylinder when completely submerged, where the vertical force

needs to be deducted from the static buoyancy experienced by the cylinder at the initial moment, as shown in Equations (7) and (8):

$$F_x{}' = \frac{4F_x}{\rho g \pi D^2 l} \tag{7}$$

$$F_z{}' = \frac{4F_z}{\rho g \pi D^2 l} \tag{8}$$

Based on the aforementioned verification, cell 2 and a time step of 0.002 s are selected for numerical wave simulation. The simulated wave is a fifth-order wave with a period of 1.29 s and a wave height of 0.075 m. The comparison between the calculated and theoretical values is depicted in Figure 5. It is evident from the figure that the simulated values closely align with the theoretical values, thus affirming the accuracy of the model.

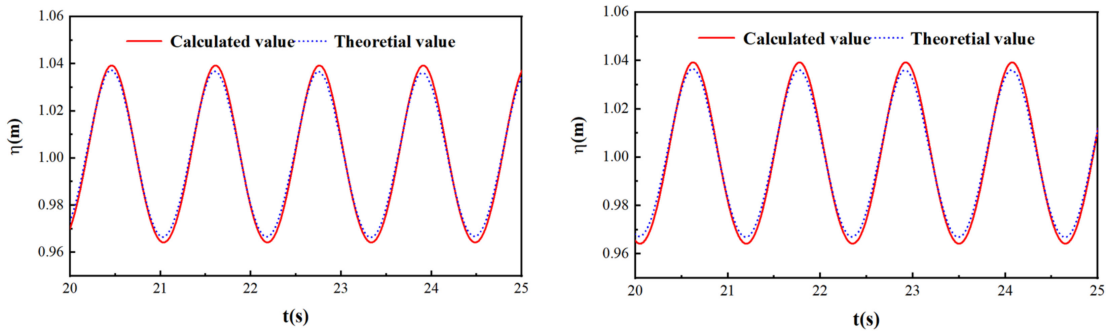

(**a**) Wave altimeter 1 (**b**) Wave altimeter 2

Figure 5. Comparison of calculated and theoretical values.

By selecting several cycles, the numerical results of the force acting on the cylinder are compared with the experimental results, as shown in Figure 6; it was found that the model has a high degree of agreement with the publicly available experimental data, proving that it exhibits good computational accuracy for calculating the wave and current forces acting on a partially submerged horizontal cylinder.

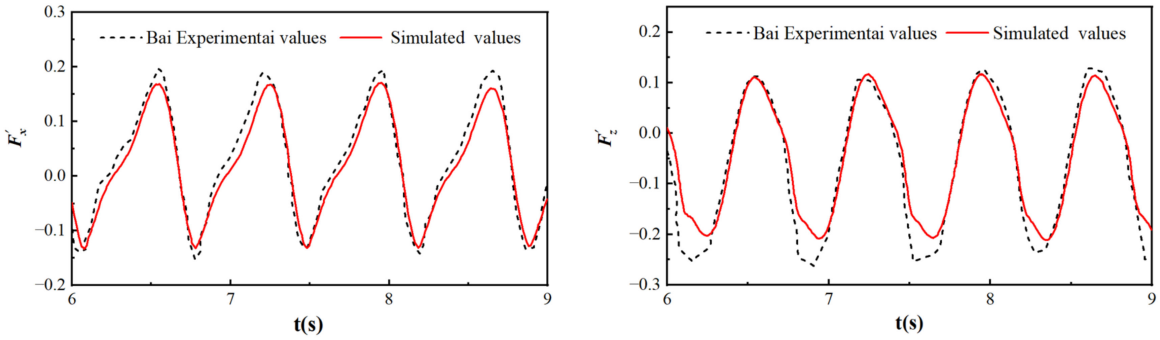

(**a**) Horizontal wave current force (**b**) Vertical wave current force

Figure 6. Wave current force on a horizontal cylinder.

2.5. Equation of Cylindrical Motion

This paper investigates the dynamic characteristics of a cylinder undergoing lateral vibration in uniform flow. Using the overlapping grid of the STAR-CCM+ 2021.1 software and combining it with the field function to simulate the lateral vibration of a cylinder, the motion under different submergence depths and amplitudes is simulated by changing the field function of the overlapping grid motion. The inflow velocity passing through a cylinder is U, and the fluid density and motion viscosity coefficient are ρ and ν, respectively.

The direction of inflow is from left to right; the corresponding coordinate system is set as x, parallel to the direction of inflow, and z, perpendicular to the direction of inflow velocity. The main consideration of this study is a cylinder with a diameter, D, of 0.1 m; a cylinder density 1.2 times that of the fluid; and a water depth, d, of 1 m. A spring damping system is used to control the undulating motion of a cylinder at different submergence depths and flow velocities; its motion equation can be expressed as:

$$m\ddot{z} + c\dot{z} + kz = F_z \tag{9}$$

where z is the displacement of the object perpendicular to the direction of flow; m, c, and k are the mass, damping, and spring stiffness coefficients per unit length of the cylinder, respectively; and F_z is the hydrodynamic force of the z-coordinate axis.

2.6. Energy Capture Efficiency

In the process of flow-induced vibration, the oscillator is subjected to three forces in the vertical direction—spring tension pressure, F_{spr}; structural and water flow resistance, F_{damp}; and fluid dynamic pressure, F_{Fluid}.

When the oscillator is below the equilibrium position and the direction of motion is downward, its acceleration direction is upward. Therefore, the following equation can be obtained:

$$m_{osc}a + F_{spr} + F_{damp} = F_{Fluid} \tag{10}$$

By reorganizing the above, the following equation can be obtained:

$$(m_{osc} + m_a)Y'' + (c_{fluid} + c_{structure})Y' + KY = \frac{\rho U \Gamma \cos(2\pi f_{st} t)}{2} \tag{11}$$

where c_{fluid} is the additional damping of the fluid; $c_{structure}$ is the total damping of the vibrating structure; Γ is the intensity of discrete point vortices; U is the inflow velocity; D and L are the diameter and length of the cylindrical oscillator, respectively; and m_a is the additional mass of the oscillator.

Moving the additional damping term of the fluid from the above equation to the right side of the equation yields the following:

$$(m_{osc} + m_a)y'' + c_{structure}y' + Ky = \frac{\rho U \Gamma \cos(2\pi f_{st} t)}{2} - c_{fluid}y'm_a \tag{12}$$

The right side of the above equation represents the difference between flow force and fluid friction, which is equal on both sides. Therefore, the left side can be integrated to obtain the energy captured by the vibration system; this can then be divided by the duration of the cycle to obtain the average effective power of the fluid. The calculation of its energy and power is as follows:

$$P_{Mesh} = \frac{1}{T_{osc}} \int_0^{T_{osc}} ((m_{osc} + m_a)y'' + c_{structure}y' + Ky)y' dt \tag{13}$$

According to the theory of harmonic motion, the displacement, y, of the oscillator exhibits a harmonic change over time, i.e., $y = A\sin(2\pi f_{osc} t)$. The main frequency of vibration of the oscillator is f_{osc} and its value is $T_{osc} = 1/f_{osc}$. In stable vibration, the liquid resonates with the oscillator. According to the law of structural dynamics resonance, the main frequency of vibration is equal to the main frequency of lift, i.e., $f_{osc} = f_{Fluid}$.

$$\begin{aligned} P_{\text{Mesh}} &= \frac{1}{T_{\text{osc}}} \int_0^{T_{\text{ose}}} c_{\text{structure}}\, y'^2 \, \mathrm{d}t = \\ &\frac{1}{T_{\text{osc}}} \int_0^{T_{\text{ose}}} c_{\text{structure}}\, 4\pi^2 f_{\text{osc}}^2\, A^2 \cos^2(2\pi f_{\text{osc}}\, t)\mathrm{d}t = 2\pi^2 f_{\text{osc}}^2\, A^2 c_{\text{structure}} \end{aligned} \tag{14}$$

The ratio of the energy harvesting power of the oscillator to the fluid loss power is defined as the energy harvesting efficiency, expressed as follows:

$$\eta = \frac{P_{\text{Mesh}}}{P_{\text{Fluid}}} = \frac{2\pi^2 f_{\text{osc}}^2 A^2 c_{\text{structure}}}{\frac{1}{2}\rho U^3 (2A + D)L} = \frac{4\pi^4 \xi (m^* + 1)(f^* A^*)^2}{U_r^3 (2A^* + 1)} \quad (15)$$

where m^* represents the mass ratio; ξ indicates the damping ratio; A^* represents the amplitude ratio; f^* represents the frequency ratio; and U_r represents the reduction speed.

3. Analysis of Calculation Results

3.1. Example Setting and Calculation Parameters

The horizontal position and grid of the cylinder, as per the numerical calculations, are shown in Figures 1 and 2. The ratio of the distance from the center of the cylinder to the static water surface to the diameter of the cylinder is $S/D = -5$~0; the water depth is d = 1 m; the radius of the cylinder is R = 0.035 m~0.065 m; and the damping ratio is 0.02, which remains unchanged. Multiple flow velocities are selected, Ur = 1.445~3.372. In numerical calculations, the grid division is set to perform multi-layer refinement near the free surface, and 200 grids are divided around the cylinder. The thickness of the boundary layer closest to the cylinder is $D/1000$ m. For the convenience of subsequent analysis, the fluid loads in this paper are all dimensionless and are treated using empirical formulas that do not consider the free surface; additionally, the force values are all average forces. The dimensionless calculation formula is as follows:

$$C_L = \frac{2F_l}{\rho U^2 D} \quad (16)$$

$$C_D = \frac{2F_d}{\rho U^2 D} \quad (17)$$

where F_d represents the fluid load of the x-coordinate axis on the cylinder; F_l is the fluid load of the z-coordinate axis on the cylinder, and is the value after deducting the initial static buoyancy.

3.2. Load Analysis of Waves and Flows on Fixed Cylinders

3.2.1. Analysis of the Force Acting on a Fixed Cylinder under Different Submergence Depths

Figure 7 shows the resistance coefficient curves of a cylinder at different submergence depths, with R = 0.05 m, T = 1.29 s, and Ur = 2.408. From the graph, it can be seen that as the submergence depth increases, the resistance coefficient first increases and then decreases. When $S/D = 0$, although the cylinder is in a semi-submerged state, the calculated resistance coefficient is relatively high under the action of waves. When $S/D = -0.5$, the cylinder is tangent to the free surface and is subjected to the combined action of waves and currents. At this time, both the horizontal force on the cylinder and the resistance coefficient are the highest. When $S/D = -1$ or -2, the cylinder is far from the free surface, which weakens the influence of waves on the cylinder, significantly reducing the drag coefficient.

Figure 8 shows the lift coefficient curves of a cylinder at different submergence depths, with R = 0.05 m, T = 1.29 s, and Ur = 2.408. From the graph, it can be seen that when $S/D = 0$ or -0.5, the lift coefficient is mostly negative, meaning that the cylinder is subjected to an upward force. This is because only a portion of the flow above the cylinder passes through, and an upward force is generated under the impact of the flow below. When $S/D = -1$ or -2, the cylinder is a certain distance from the free surface, and the lift coefficient fluctuates around 0, weakening the influence of the free surface and waves.

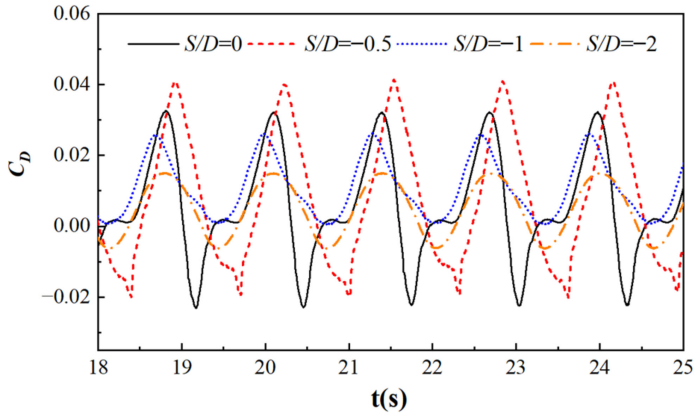

Figure 7. Resistance coefficient diagram under different submergence depths.

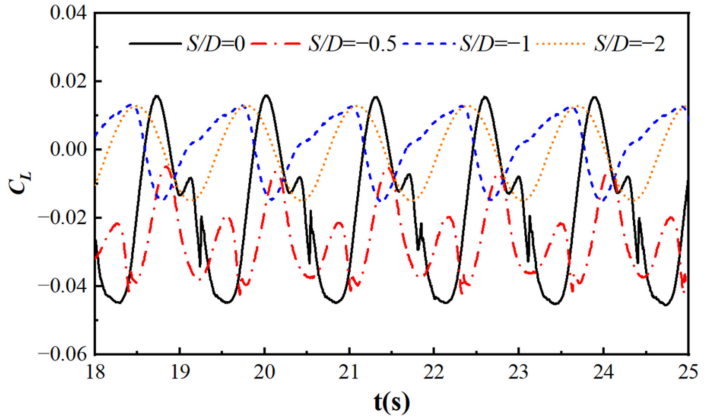

Figure 8. Lift coefficient diagram under different submergence depths.

3.2.2. Analysis of the Force Acting on a Fixed Cylinder under Different Wave Conditions

Figure 9 shows the resistance coefficient curves of a cylinder at different flow velocities, with R = 0.05 m, T = 1.29 s, and S/D = −2. From the graph, it can be seen that as the flow velocity increases, the resistance coefficient gradually decreases. When Ur = 1.445, the resistance coefficient changes significantly, and the force on the cylinder is affected by the combined effects of waves and currents. Only the flow velocity is dimensionless, resulting in a larger calculation result. When Ur = 1.926~3.372, the increase in flow velocity significantly reduces the impact of wave blockage. After the non-dimensionalization of flow velocity, the larger the flow velocity, the smaller the resistance coefficient. It can be seen that flow velocity plays an important role in the horizontal force of the cylinder.

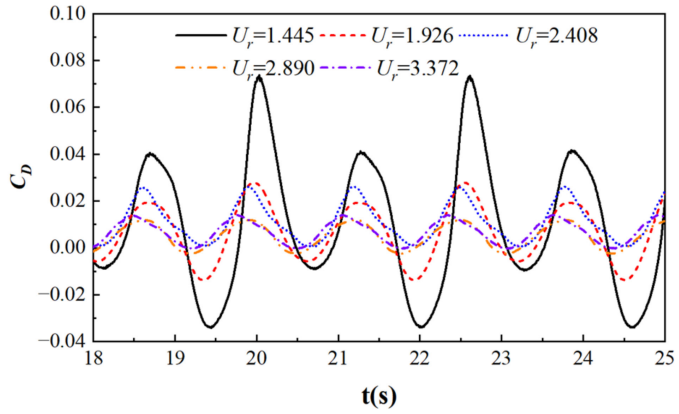

Figure 9. Resistance coefficient diagram under different flow velocities.

Figure 10 shows the lift coefficient curves of a cylinder at different flow velocities, with R = 0.05 m, T = 1.29 s, and S/D = −2. From the graph, it can be seen that as the flow velocity increases, the lift coefficient gradually decreases and fluctuates around 0. When Ur = 1.445, the lift coefficient is large, and the cylinder is affected by the combined effects of waves and currents. Only the flow velocity is dimensionless, resulting in a larger calculation result. When Ur = 1.926~3.372, the period of the lift coefficient curve is significantly reduced compared to the case when Ur = 1.445, mainly due to the dimensionless formula.

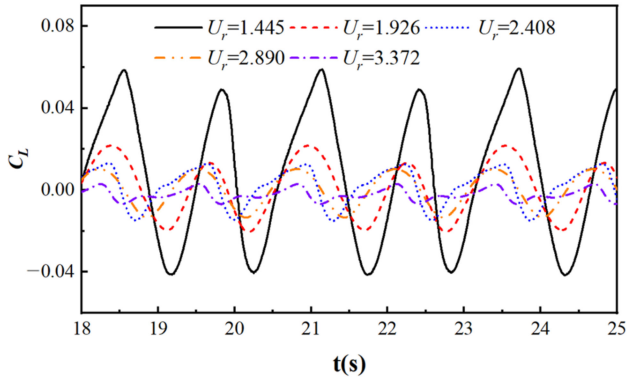

Figure 10. Lift coefficient diagram under different flow velocities.

Figure 11 shows the resistance coefficient curves of a cylinder under different wave periods, with R = 0.05 m, Ur = 2.408, and S/D = −2. From the graph, it can be seen that as the wave period increases, the drag coefficient does not change much. When T = 1.15 s, due to wave reflection and wave blocking, the resistance curve is not smooth, and the wave blocking effect begins to increase after 23 s. When T = 1.29 s or 1.45 s, the drag coefficient is also affected by wave reflection, but the effect is weaker compared to the case when T = 1.15 s; additionally, wave blockage does not increase significantly with time. When T = 1.2 s or 1.35 s, the overall coefficient is lower compared to that in other situations.

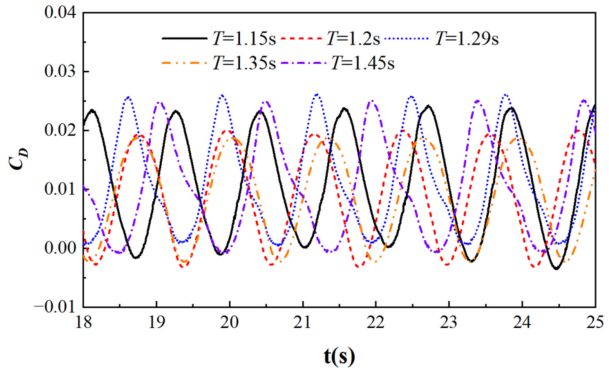

Figure 11. Resistance coefficient diagram under different wave periods.

Figure 12 shows the lift coefficient curves of a cylinder under different wave periods at R = 0.05 m, Ur = 2.408, and S/D = −2. From the graph, it can be seen that as the wave period increases, the lift coefficient gradually decreases, and the change is significant at T =1.15 s. At this time, the waves are steeper, and the interference on the flow velocity is more obvious. When T is small, during the propagation of waves, the distance from the free surface above the cylinder will decrease, and the upward force of the cylinder will increase under the effect of the flow velocity below. As T increases, wave propagation slows down, and a high-speed flow zone forms between the cylinder and the free surface. As the wave period increases, the downward force will be slightly greater than the upward force.

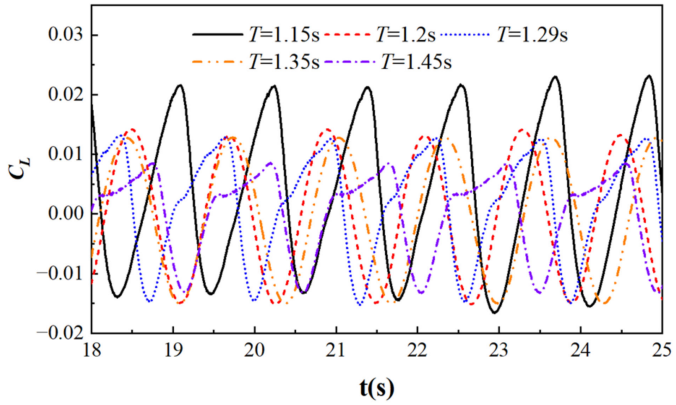

Figure 12. Lift coefficient diagram under different wave periods.

3.2.3. Analysis of the Force Acting on a Fixed Cylinder under Different Cylinder Sizes

Figure 13 shows the resistance coefficient curves of cylinders with different cylinder sizes, with T = 1.29 s, Ur = 2.408, and $S/D = -2$. From the graph, it can be seen that as the radius of the cylinder increases, the drag coefficient first decreases and then increases. When R is small, the absolute distance between the cylinder and the free surface is also small, and under the action of waves, wave reflection and blockage effects are obvious. When R = 0.05 m, the absolute distance between the cylinder and the free surface is relatively great, which weakens the wave reflection and blocking effects. When R is large, although the absolute distance between the cylinder and the free surface is also relatively large, the increase in cylinder volume intensifies the fluctuation of the free surface under the impact of flow velocity.

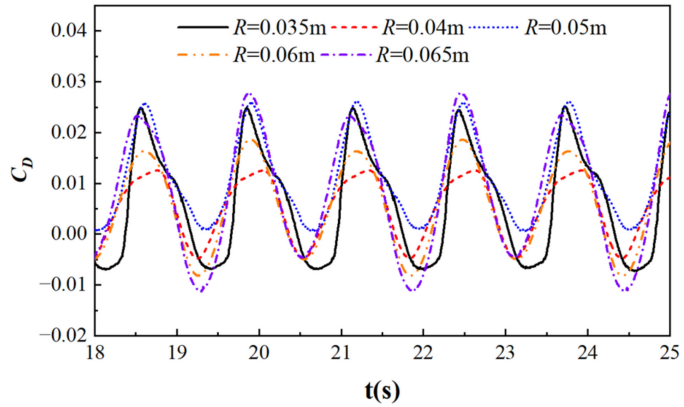

Figure 13. Resistance coefficient diagram under different cylinder radii.

Figure 14 shows the lift coefficient curves of a cylinder with different cylinder sizes, with T = 1.29 s, Ur = 2.408, and $S/D = -2$. From the graph, it can be seen that as the radius of the cylinder increases, the lift coefficient gradually increases. When R is small, the maximum lift coefficient fluctuates due to the absolute distance between the free surface and the liquid surface, which is affected by wave propagation. As the R value increases, the lift curve becomes smoother and is more affected by the flow velocity than by the waves.

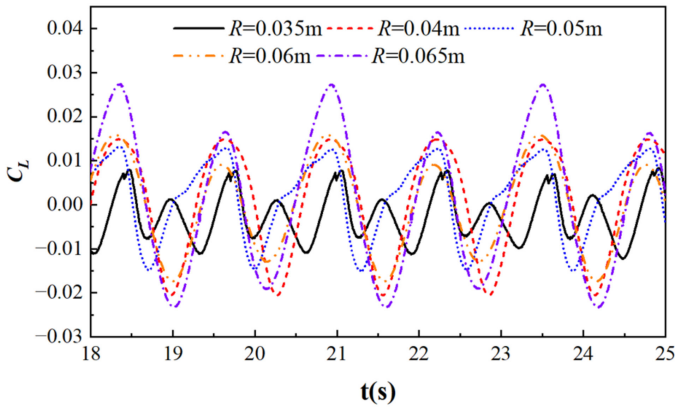

Figure 14. Lift coefficient diagram under different cylinder radii.

3.3. Displacement Analysis of Rotating Cylinders by Waves and Flows

Figure 15 shows the vibration response and Fourier transform curves of a cylinder at different flow velocities, with R = 0.05 m, $S/D = -2$, T = 1.29 s, k = 2 N/m, and $L = 2D$. From the graph, it can be seen that the larger the flow velocity, the greater the vibration amplitude; the main frequency is effectively the same under different reduced velocities. When Ur = 1.445, the flow velocity is small, resulting in a lower amplitude of cylindrical vibration, which is approximately 0.05 m. When Ur = 2.408, the increase in flow velocity leads to an increase in the vertical force of the cylinder and its displacement; the downward displacement is higher than the upward displacement. When Ur = 3.372, the amplitude of cylindrical vibration increases significantly, about twice that of the case when Ur = 1.445, while the main frequency of vibration remains unchanged. At different flow velocities, the vortex leakage frequency varies, ultimately affecting the vibration amplitude.

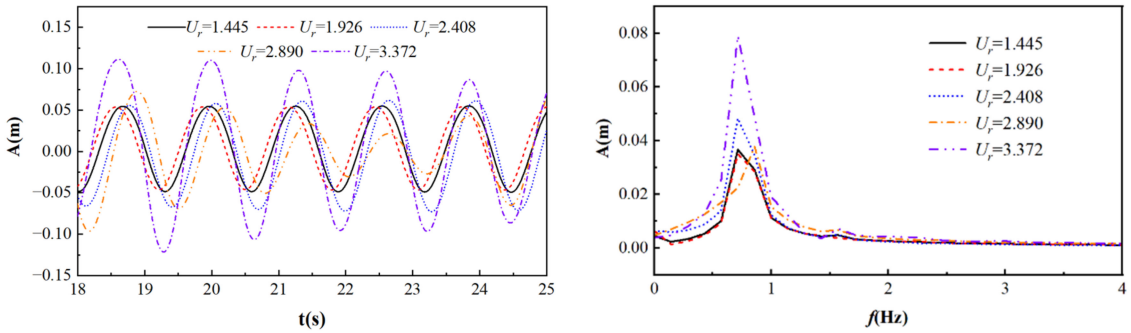

Figure 15. Cylindrical motion curves at different flow velocities.

Figure 16 shows the vibration response and Fourier transform curves of a cylinder with different arm lengths at R = 0.05 m, $S/D = -2$, T = 1.29 s, k = 2 N/m, and Ur = 2.408. From the graph, it can be seen that both short and long force arms can cause instability in the movement of the cylinder. The main frequencies are similar under different arm lengths. When $L = 1.5D$, the force arm is shorter, and the rotation angle of the cylinder during vibration is larger. The displacement is smaller under the influence of the force arm. When $L = 2.25D$, the cylindrical vibration curve is relatively stable and reaches its maximum value. When $L = 2.5D$, as the length of the force arm continues to increase, the rotation point is further away, the rotational resistance increases, and the cylindrical displacement begins to decrease; the main frequency does not change with the size of the force arm.

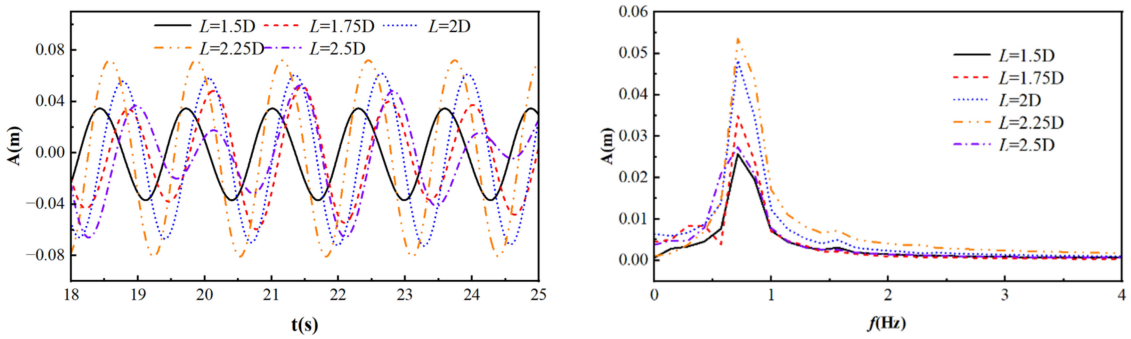

Figure 16. Cylindrical rotation motion curves under different moment arms.

Figure 17 shows the vibration response and Fourier transform curves of a cylinder under different wave periods at R = 0.05 m, S/D = −2, Ur = 2.408, k = 2 N/m, and L = 2D. From the graph, it can be seen that the larger the period, the greater the vibration amplitude; its corresponding main frequency gradually shifts to the left. When T = 1.15 s, the amplitude of cylindrical vibration is lower, with a maximum amplitude of about 0.05 m. When T = 1.29 s and T = 1.45 s, the amplitude of cylindrical vibration increases with an increase in wave period, the main frequency shifts to the left with an increase in wave period, and the high-frequency characteristics become more obvious.

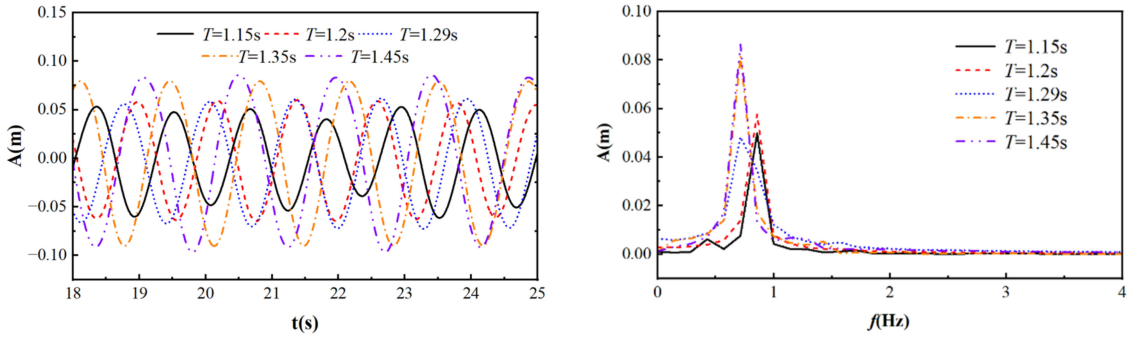

Figure 17. Cylindrical rotating motion curves at different periods.

Figure 18 shows the vibration response and Fourier transform curve of a cylinder at different k values at the rotation point, with R = 0.05 m, S/D = −2, T = 1.29 s, Ur = 2.408, and L = 2D. From the graph, it can be seen that the larger the k value, the larger the vibration amplitude; additionally, the high-frequency characteristics begin to increase. When k = 1.5 N/m, the torque is smaller, and the force arm has a lower limit on the rotation of the cylinder. When k = 2 N/m, the increase in torque leads to an increase in vibration amplitude under the action of waves and currents. When k = 2.25 N/m, the torque continues to increase and reaches its maximum, and the curve of the cylindrical vibration response becomes smoother and more regular. As the k value continues to increase, the displacement slightly decreases.

Figure 19 shows the vibration response and Fourier transform curves of a cylinder with different cylinder radii, with T = 1.29 s, S/D = −2, Ur = 2.408, k = 2 N/m, and L = 2D. From the graph, it can be seen that the main frequency remains effectively unchanged at different radii, and that the amplitude first increases and then decreases with the increase in cylinder radius. When R = 0.035 m, the radius is smaller, making the vibration amplitude of the cylinder more complex under the influence of wave currents. When R = 0.05 m, the vibration amplitude increases significantly, and its motion period is relatively stable. As the R value continues to increase, the amplitude of the cylindrical vibration response begins to decrease. The further increase in the radius of the cylinder leads to an increase in the overall mass, the absolute depth of submergence, and the absolute length of the force arm, while the amplitude slightly decreases.

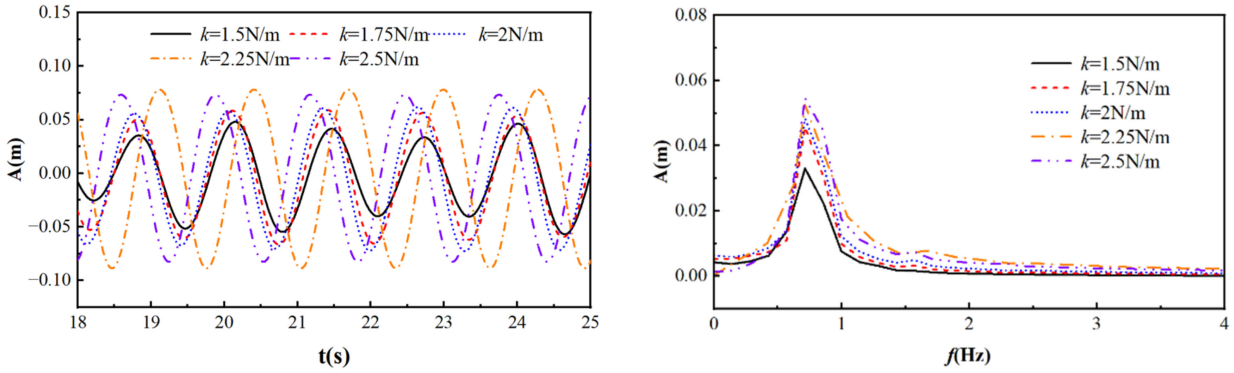

Figure 18. Curve of rotation motion of cylinder under different torques.

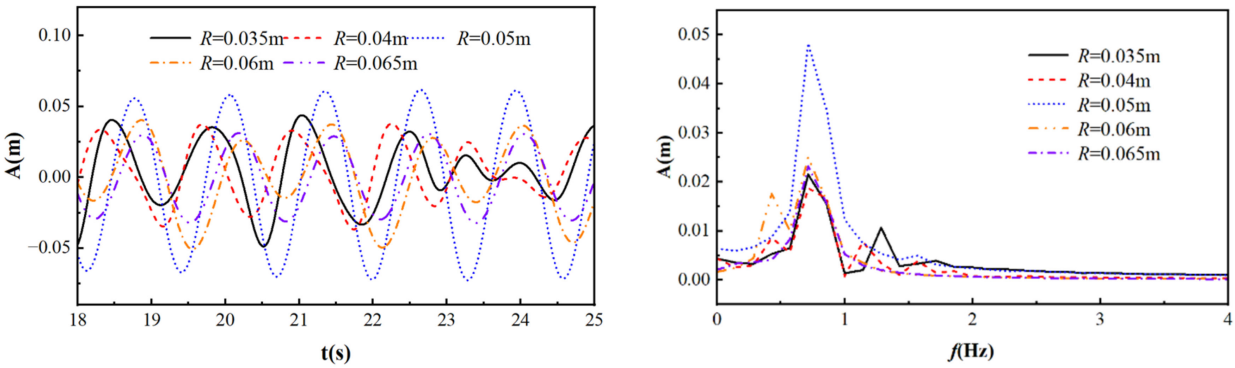

Figure 19. Cylindrical rotation motion curves with different radii.

3.4. Analysis of the Interaction Flow Field between Waves and Rotating Cylinders

The flow field diagram, velocity diagram, and vorticity diagram of a rotating cylinder under wave and current conditions were analyzed. Figure 20 shows both the flow field and flow velocity diagrams, as well as their corresponding vorticity changes, with R = 0.05 m, $S/D = -2$, T = 1.29 s, M = 0.08 N/m, $L = 2D$, and Ur = 2.408, which clearly shows the changes in the interaction between the wave and the cylinder.

From the flow field diagram, it can be seen that the cylinder moves up and down under the combined action of waves and currents, while the free surface directly above the cylinder experiences fluctuations due to the movement of the cylinder. From the flow velocity chart, it can be seen that, when there is a trough above the cylinder, the flow velocity around it is lower. When the peak arrives, the flow velocity above and below the cylinder increases rapidly, while the flow velocity in front and behind the cylinder remains lower. When the trough temporarily decreases again, the flow velocity around the cylinder also decreases. Overall, when the peak is close to the cylinder above, the flow velocity around the cylinder is higher; however, when the trough is close to the cylinder above, the flow velocity around the cylinder is lower. From the vorticity plot, it can be seen that vortex shedding occurs under the influence of flow velocity on the cylinder itself; it also occurs during the rotation of the cylinder. Combined with the analysis of the flow velocity plot, when the wave peak is close to the top of the cylinder, the surrounding flow velocity increases, accelerating vortex shedding. When the wave trough is close to the top of the cylinder, the flow velocity around the cylinder is relatively low, reducing the vortex shedding phenomenon of the cylinder.

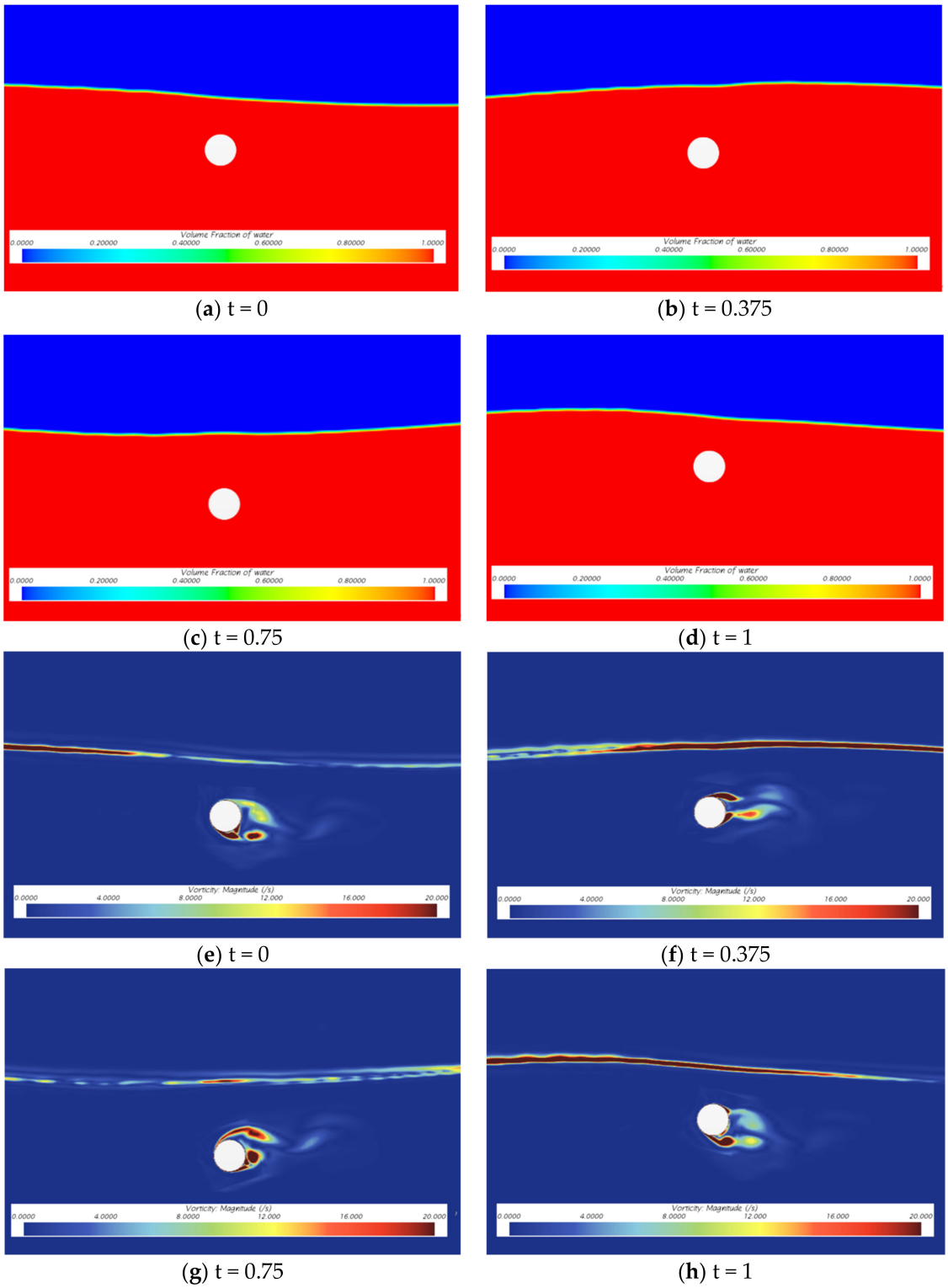

Figure 20. Flow field diagram and vorticity diagram of cylinder movement in one cycle.

3.5. Analysis of Fluid Load on Rotating Cylinders

3.5.1. Fluid Load Analysis under Different Wave Conditions

Figure 21 shows the resistance coefficient curves of a rigid rotating cylinder at different flow velocities, with $S/D = -2$, $R = 0.05$ m, $T = 1.29$ s, $k = 2$ N/m, and $L = 2D$. From the graph, it can be seen that as the flow velocity increases, the resistance coefficient gradually decreases, and the horizontal force of waves on the cylinder plays an important role. After

the dimensionless transformation of the flow velocity, the following results are obtained: when Ur = 1.445 or 1.926, the flow velocity is small, and the cylinder is subjected to a smaller horizontal force from the ocean current. During the rotation of the cylinder, significant fluctuations occur in the free surface, and wave reflection and blockage cause fluctuations in the resistance coefficient. When Ur = 2.890 or 3.372, the flow velocity is relatively high, and the proportion of flow velocity in the comprehensive influence of the wave and current increases, resulting in a decrease in the overall coefficient after dimensionless transformation, as well as a significant reduction in the wave blockage effect.

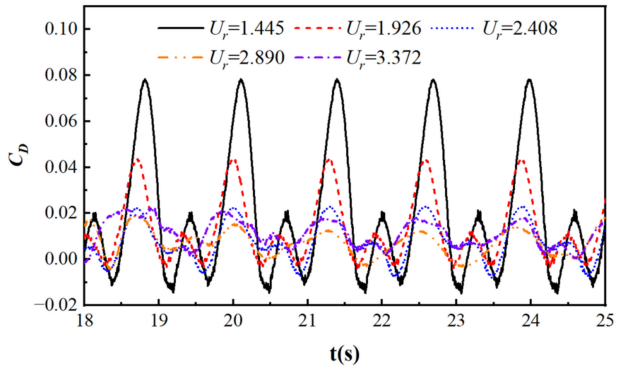

Figure 21. Cylindrical resistance coefficient curves at different reduction speeds.

Figure 22 shows the lift coefficient curves of a rigid rotating cylinder at different flow velocities, with $S/D = -2$, R = 0.05 m, T = 1.29 s, k = 2 N/m, and $L = 2D$. From the graph, it can be seen that as the flow velocity increases, the lift coefficient gradually decreases, the impact of wave blockage on the cylinder decreases, and the curve becomes smoother. When Ur = 1.445, both the flow velocity and the vertical force from the ocean current on the cylinder are small. Under the combined action of waves and currents, the proportion of the waves is high, resulting in a larger lift coefficient after dimensionless transformation. When Ur = 3.372, the higher the flow velocity, the greater the vertical force of the ocean current and the higher the proportion of the ocean current, under the combined action of waves and currents.

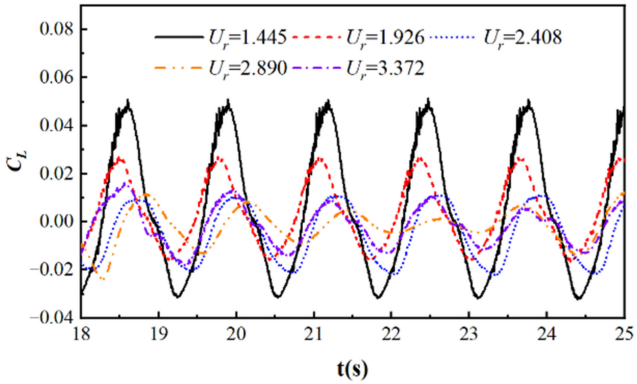

Figure 22. Cylinder lift coefficient curves at different reduction speeds.

Figure 23 shows the resistance coefficient curves of a rigid rotating cylinder under different wave periods, with $S/D = -2$, R = 0.05 m, Ur = 2.408, k = 2 N/m, and $L = 2D$. From the graph, it can be seen that the rotation of a rigid cylinder has a significant impact on wave reflection and blockage at different wave periods. The curve becomes rough, and the larger the wave period, the higher the resistance coefficient. When T = 1.15 s, the period is small and is greatly affected by the rotation of the cylinder, resulting in the most unstable change in the resistance coefficient. When T = 1.45 s, the period is relatively large, and the wave propagation process is relatively smooth. The reflection generated by the rigid

rotating cylinder has an impact on the characteristics of the wave, and at some points, the variation of the cylinder's resistance coefficient is more complex.

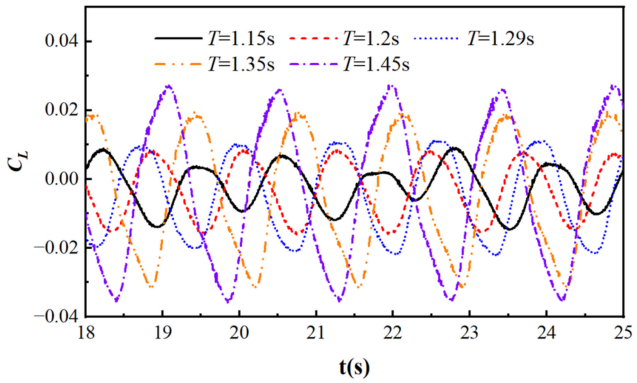

Figure 23. Cylindrical resistance coefficient curves under different wave periods.

Figure 24 shows the lift coefficient curves of a rigid rotating cylinder under different wave periods, with $S/D = -2$, $R = 0.05$ m, $Ur = 2.408$, $k = 2$ N/m, and $L = 2D$. From the graph, it can be seen that as the wave period increases, its lift coefficient gradually increases and the periodicity of its lift curve becomes more pronounced. When $T = 1.15$ s, the period is small, and during the rotational motion of the cylinder, it has a significant impact on the propagation of waves, resulting in unstable changes in the resistance coefficient. When $T = 1.45$ s, the period is relatively large, and the wave propagation process is relatively smooth. The impact of the cylinder's rotational motion on the waves is relatively small, ultimately leading to an increase in the stability of the cylinder's force.

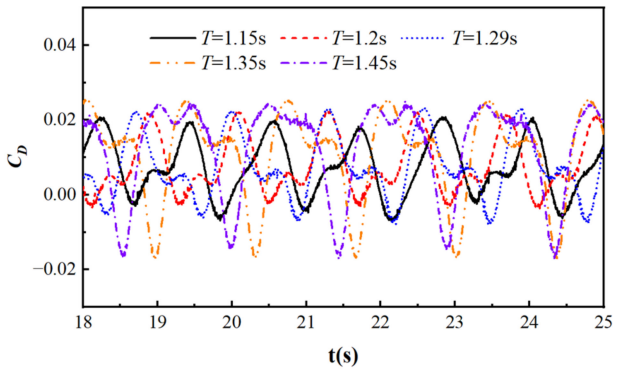

Figure 24. Lift coefficient curves of the cylinder under different wave periods.

3.5.2. Fluid Load Analysis under Different k Values

Figure 25 shows the resistance coefficient curves of a rigid rotating cylinder at different k values at the rotation point, with $S/D = -2$, $R = 0.05$ m, $T = 1.29$ s, $Ur = 2.408$, and $L = 2D$. From the graph, it can be seen that as the torque increases, the resistance coefficient gradually increases. The greater the torque, the stronger the reverse force generated, which offsets some of the forces on the cylinder and weakens the influence of the waves. When $k = 2$ N/m, the torque is small, which limits the displacement of the cylinder, and the minimum distance from the free liquid surface increases, weakening the horizontal force of the waves. When $k = 2.5$ N/m, the torque is greater, which further limits the displacement of the cylinder. The minimum distance from the free surface increases, and it is less affected by waves, leading to an increase in the resistance curve.

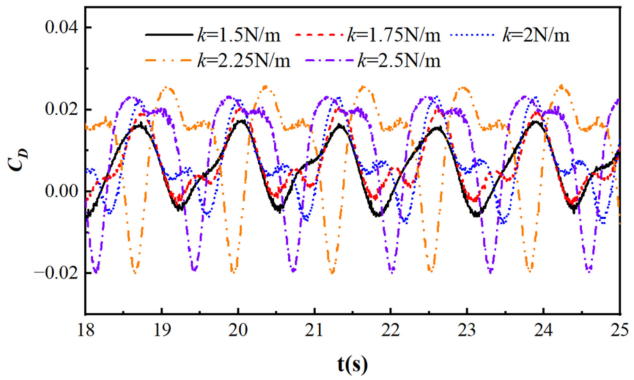

Figure 25. Cylindrical drag coefficient curves with different torques.

Figure 26 shows the lift coefficient curves of a rigid rotating cylinder at different k values at the rotation point, with $S/D = -2$, $R = 0.05$ m, $T = 1.29$ s, $Ur = 2.408$, and $L = 2D$. From the graph, it can be seen that as the value of k increases, the lift coefficient gradually increases. When $k = 1.5$ N/m, the value of k is small, the amplitude of cylindrical motion is large, and the change in the lift coefficient is unstable. When $k = 2$/m, as the value of k increases, its lift coefficient becomes relatively stable, and the impact of reflection caused by cylinder blockage on wave characteristics weakens. As the value of k continues to increase, its lift curve becomes smoother.

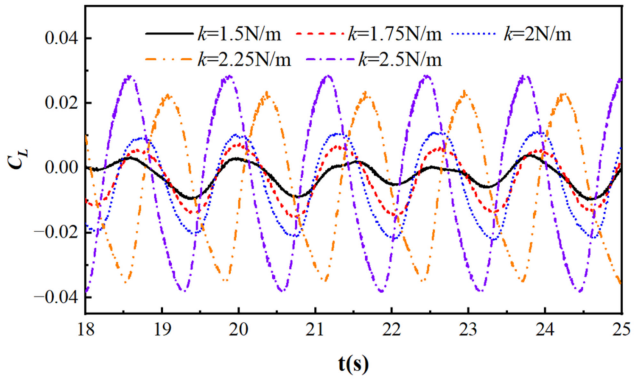

Figure 26. Lift coefficient curves of cylinders with different torques.

3.5.3. Fluid Load Analysis under Different Cylinder Radii

Figure 27 shows the resistance coefficient curves of a rigid moving cylinder under different cylinder radii, with $S/D = -2$, $k = 2$ N/m, $T = 1.29$ s, $Ur = 2.408$, and $L = 2D$. From the graph, it can be seen that as the radius of the cylinder increases, the overall trend first increases and then decreases; the drag coefficients are all unstable. When $R = 0.035$ m, the radius of the cylinder is small, the absolute distance from the free surface is relatively short, and it is strongly affected by wave currents, so its resistance curve is extremely unstable. When $R = 0.05$ m, compared to $R = 0.035$ m, the curve is relatively stable and has a certain regularity. As the radius continues to increase, the resistance coefficient begins to decrease.

Figure 28 shows the lift coefficient curves of a moving cylinder at different cylinder radii, with $S/D = -2$, $k = 2$ N/m, $T = 1.29$ s, $Ur = 2.408$, and $L = 2D$. From the graph, it can be seen that as the radius of the cylinder increases, the overall trend gradually decreases. When $R = 0.035$ m, the radius of the cylinder is smaller, the absolute distance from the free surface is shorter, and it is strongly affected by wave currents, so its lift curve is more complex. When $R = 0.05$ m, compared to $R = 0.035$ m, the curve is relatively stable, and as the radius continues to increase, the lift coefficient becomes unstable again.

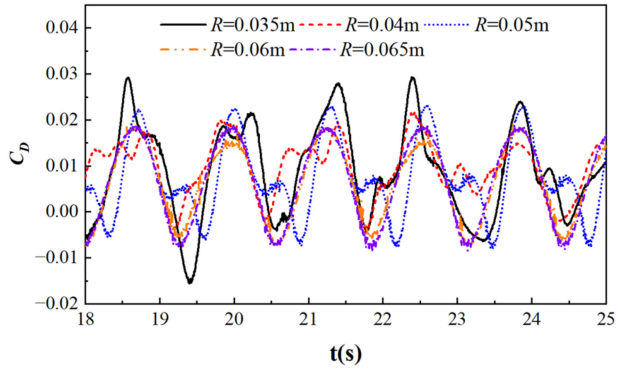

Figure 27. Cylindrical resistance coefficient curves with different cylindrical radii.

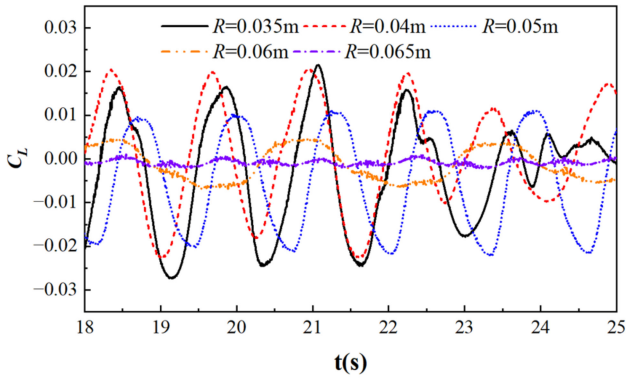

Figure 28. Lift coefficient curves of cylinders with different cylindrical radii.

3.5.4. Fluid Load Analysis under Different Arm Lengths

Figure 29 shows the resistance coefficient curves of a rigid rotating cylinder under different arm lengths, with $S/D = -2$, $R = 0.05$ m, $T = 1.29$ s, $k = 2$ N/m, and $Ur = 2.408$. From the graph, it can be seen that as the length of the lever arm increases, the resistance coefficient of the cylinder gradually increases. When $L = 1.5D$, the rotation angle of the cylinder is relatively large. Driven by the rotation of the cylinder, the wave blocking effect increases, weakening the influence of the horizontal force from the wave flow. When $L = 2.5D$, the length of the force arm increases, the rotation angle and wave blocking effect decrease, and the drag coefficient increases.

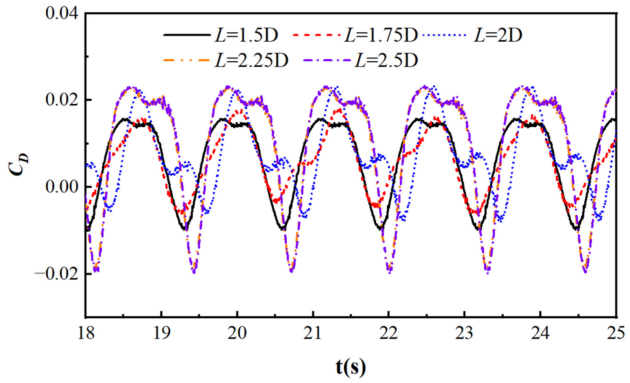

Figure 29. Cylindrical resistance coefficient curves at different moment arm lengths.

Figure 30 shows the lift coefficient curves of a rigid rotating cylinder under different arm lengths, with $S/D = -2$, $R = 0.05$ m, $T = 1.29$ s, $k = 2$ N/m, and $Ur = 2.408$. From the graph, it can be seen that as the length of the lever arm increases, the negative lift coefficient gradually increases and the positive lift coefficient gradually decreases. When $L = 1.5D$, the

rotation angle of the cylinder is larger, the rotation speed of the cylinder is greater, and its lift coefficient is not periodic, making it more complex. When $L = 2.5D$, the length of the lever arm increases, the rotation angle decreases, and the lift coefficient becomes regular and predictable.

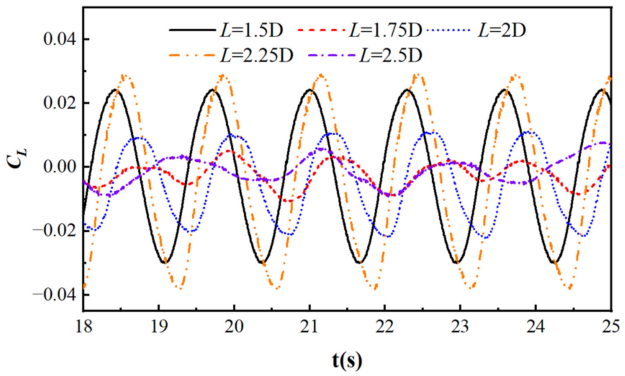

Figure 30. Lift coefficient curves of the cylinder with different moment arm lengths.

3.6. Calculation of Energy Harvesting Efficiency of a Cantilever Cylinder Rotating around an Axis under Wave Current Conditions

Figure 31 shows the bar graph of the energy harvesting efficiency of a rotating cylinder under different spring stiffness values *(k)*, with $S/D = -2$, $T = 1.29$ s, $R = 0.05$ m, $Ur = 2.408$, and $L = 2D$. From the graph, it can be seen that as the value of k increases, the energy harvesting efficiency of the rotating cylinder first increases and then decreases. When $k = 1.5$ N/m, the value of k is small, the torque on the cylinder is less restrictive, the amplitude of cylinder motion is higher, and the displacement is larger, resulting in a lower energy harvesting efficiency, despite it being the highest total energy harvesting recorded. When $k = 2.25$ N/m, as the value of k increases, the amplitude of cylindrical motion decreases, the energy captured in the region decreases, and the total energy also decreases accordingly; the calculated energy capture efficiency is the highest. When $k = 2.5$ N/m, the further increase in k value greatly limits the motion amplitude, reduces the displacement of cylindrical motion, and significantly reduces its energy capture, ultimately leading to a decrease in energy capture efficiency.

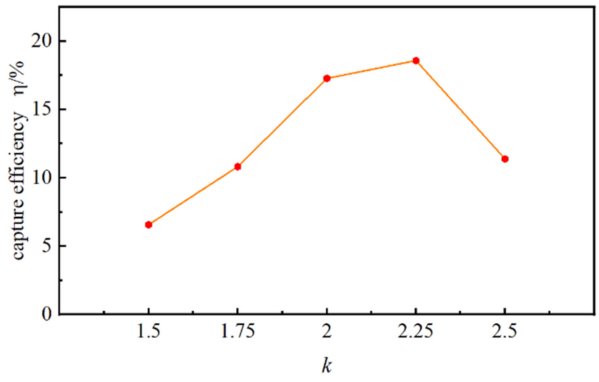

Figure 31. Energy capture efficiency of a rotating moving cylinder under different k values.

Figure 32 shows the bar graph of the energy capture efficiency of a moving cylinder at different flow velocities, with $S/D = -2$, $R = 0.05$ m, $k = 2$ N/m, $T = 1.29$ s, and $L = 2D$. From the graph, it can be seen that as the flow velocity increases, the energy capture efficiency of the rotating cylinder gradually decreases. Under the joint action of waves and currents, the displacement of the cylinder caused by the flow velocity is not significant, resulting in a low energy capture efficiency in the calculation results. When $Ur = 1.445$, the flow velocity is small, and the influence of waves on the displacement of the cylinder is relatively

high. When the flow velocity is non-dimensionalized, its numerical value is higher. When Ur = 2.408, as the flow velocity increases, the amplitude of cylindrical motion does not increase significantly, and the energy efficiency captured in the region decreases. When Ur = 3.372, as the flow velocity continues to increase, although the motion amplitude continues to increase, the total energy per unit time increases due to the increase in flow velocity, ultimately leading to a slight decrease in energy harvesting efficiency.

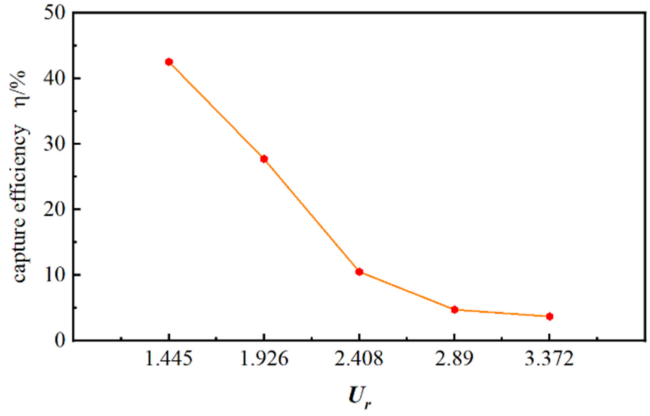

Figure 32. Energy harvesting efficiency of a rotating moving cylinder at different reduction speeds.

Figure 33 shows the bar graph of the energy capture efficiency of a moving cylinder under different wave periods, with $S/D = -2$, R = 0.05 m, k = 2 N/m, Ur = 2.408, and $L = 2D$. From the graph, it can be seen that as the wave period increases, the energy capture efficiency of the rotating cylinder first increases and then decreases. When T = 1.15 s, the wave period is small, the amplitude curve of the cylinder's motion is stable, and the vibration amplitude is large, resulting in a higher energy capture efficiency. When T = 1.29 s, with the increase in wave period, the amplitude of cylindrical motion decreases, and the periodicity of motion becomes less obvious. The energy captured in the region decreases significantly, but the calculated energy capture efficiency is at its highest. When T = 1.45 s, as the wave period continues to increase, although the motion period becomes unstable, the maximum amplitude of the motion increases significantly, ultimately leading to an increase in energy capture efficiency, but this is less than is the case when T = 1.15 s.

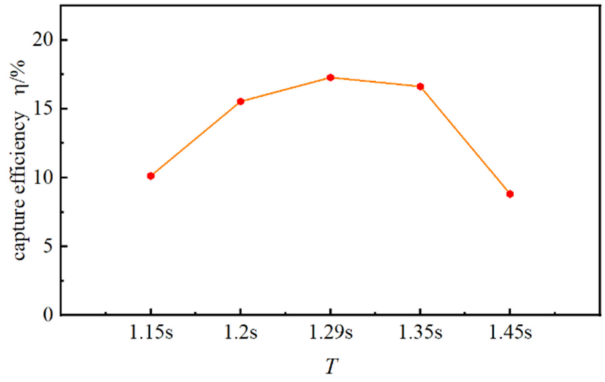

Figure 33. Energy harvesting efficiency of a rotating cylinder under different wave periods.

Figure 34 shows the bar graph of the energy capture efficiency of a moving cylinder under different arm lengths, with $S/D = -2$, R = 0.05 m, k = 2 N/m, and Ur = 2.408. From the graph, it can be seen that as the length of the force arm increases, the energy harvesting efficiency first increases and then decreases. When $L = 1.5D$, the force arm is shorter, the angle of cylindrical axis motion is larger, and the amplitude of the motion curve is lower, resulting in a lower energy harvesting efficiency. When $L = 2.25D$, as the length of the lever arm increases, the amplitude of the cylindrical motion slightly increases, and the periodicity

of the motion becomes apparent, with the highest proportion of energy being captured in this region. When $L = 2.5D$, as the length of the force arm continues to increase, the motion period becomes unstable, and the motion amplitude begins to decrease, ultimately leading to a decrease in energy harvesting efficiency.

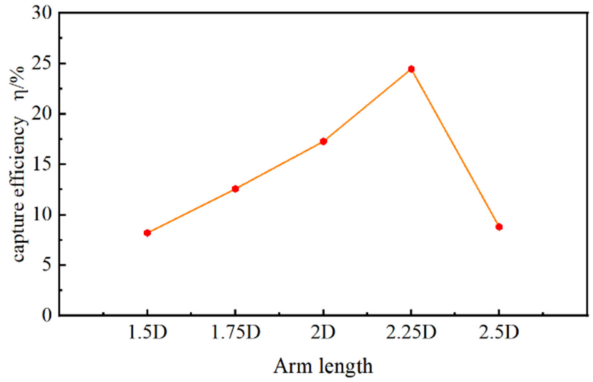

Figure 34. Energy harvesting efficiency of a rotating moving cylinder with different moment arm lengths.

Figure 35 shows the bar graph of the energy capture efficiency of a moving cylinder at different cylinder radii, with $S/D = -2$, $T = 1.29$ s, $k = 2$ N/m, $Ur = 2.408$, and $L = 2D$. From the graph, it can be seen that as the radius of the cylinder increases, the energy capture efficiency first increases and then decreases. When $R = 0.035$ m, the radius of the cylinder is small, and the displacement to radius ratio is large, resulting in a higher energy capture efficiency per unit of time. When $R = 0.05$ m, as the radius of the cylinder increases, the ratio of displacement to the radius decreases, and the energy captured in the region increases; its total energy also increases accordingly, leading to a decrease in final efficiency. When $R = 0.065$ m, the radius and the motion amplitude continue to increase, the absolute length of the force arm increases, the rotation angle decreases, and its energy harvesting efficiency is similar to that of the vertical equation.

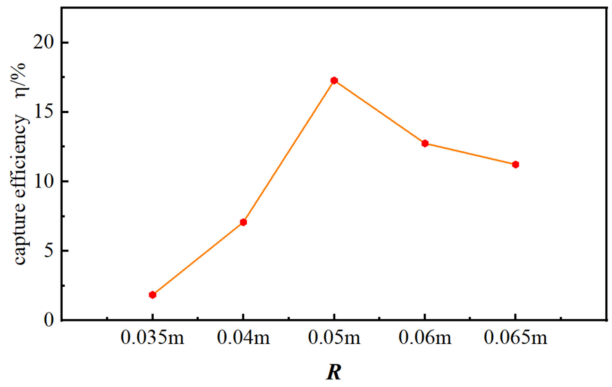

Figure 35. Energy harvesting efficiency of a rotating moving cylinder with different cylindrical radii.

4. Conclusions

Based on the CFD numerical simulation method, the load analysis of wave currents with free surfaces under different submergence depths, flow velocities, cylinder sizes, and wave periods was studied. The following conclusions were obtained by analyzing the numerical simulation results:

(1) When a cylinder approaches a free surface, its hydrodynamic load under wave current conditions is more sensitive to changes in submergence depth, which affects wave reflection and wave blockage.

(2) The main frequency of the Fourier transform of the cylindrical motion curve remains unchanged at different flow velocities, k values, force arms, and radii; the main

frequency of the Fourier transform of the cylindrical motion curve varies with the wave period and the depth of submergence.

(3) The efficiency of rotary cylindrical energy harvesting is influenced by various factors, among which an initial increase and then decrease are observed with a gradually increasing k value, arm length, period, and radius, in addition to an observed decrease with increasing flow velocity.

Author Contributions: Methodology, X.Z.; software, Q.J.; validation, K.W. and X.Z.; formal analysis, X.Z. and S.W.; investigation, Q.J.; data curation, Q.J.; writing—original draft preparation, X.Z.; writing—review and editing, S.W. All authors have read and agreed to the published version of the manuscript.

Funding: This research was funded by the National Natural Science Foundation of China (52071348 and 51979129).

Institutional Review Board Statement: Not applicable.

Informed Consent Statement: Not applicable.

Data Availability Statement: The data presented in this study are available on request from the corresponding author.

Conflicts of Interest: The authors declare no conflict of interest.

References

1. Reichl, P.; Hourigan, K.; Thompson, M. The unsteady wake of a circular cylinder near a free surface. *Flow Turbul. Combust.* **2003**, *71*, 347–359. [CrossRef]
2. Reichl, P.; Hourigan, K.; Thompson, M.C. Flow past a cylinder close to a free surface. *J. Fluid Mech.* **2005**, *533*, 269–296. [CrossRef]
3. Wu, C.S.; Young, D.L. Simulations of free-surface flows with an embedded object by a coupling partitioned approach. *Comput. Fluids* **2014**, *89*, 66–77. [CrossRef]
4. Bozkaya, C.; Kocabiyik, S.; Mironova, L.A.; Gubanov, O.I. Streamwise oscillations of a cylinder beneath a free surface: Free surface effects on vortex formation modes. *J. Comput. Appl. Math.* **2011**, *235*, 4780–4795. [CrossRef]
5. Xiao, H.; Huang, W.; Tao, J.; Liu, C. Numerical modeling of wave–current forces acting on horizontal cylinder of marine structures by VOF method. *Ocean. Eng.* **2013**, *67*, 58–67. [CrossRef]
6. Bai, J.; Ma, N.; Gu, X. Numerical study of the interaction between combined wave-current and a horizontal cylinder close to the free surface. In Proceedings of the International Ocean and Polar Engineering Conference, Rhodes, Greece, 26 June–2 July 2016.
7. Gu, M.; Song, B.; Zhang, B.; Mao, Z.; Tian, W. The effects of submergence depth on Vortex−Induced Vibration (VIV) and energy harvesting of a circular cylinder. *Renew. Energy* **2020**, *151*, 931–945. [CrossRef]
8. Zhao, W.; Wan, D.; Zhao, S. CFD simulation of two-phase flows past a surface-piercing circular cylinder. In Proceedings of the International Ocean and Polar Engineering Conference, Virtual, 11–16 October 2020.
9. Wang, Y.; Lou, M.; Liu, X. Experimental design of energy capture for cylindrical flow induced vibration under wake interference. *Lab. Res. Explor.* **2023**, *42*, 62–65.
10. Wang, C.; Lv, H.; Huang, J.; Yang, Y. Research on the interaction between second-order wave current and upright double cylinders. *J. Huazhong Univ. Sci. Technol. (Nat. Sci. Ed.)* **2023**, *51*, 135–141.
11. Zhang, X.; Huo, J.; Zhang, M.; Xie, Z. Solitary wave-current forces on a horizontal cylinder by a fourth-order-accurate finite volume compact solver. *Ocean. Eng.* **2024**, *294*, 116788. [CrossRef]
12. Lin, Z.; Zan, X. Numerical study on load characteristics by internal solitary wave on cylinder sections at different depth and its parameterization. *Ocean. Eng.* **2021**, *219*, 108343. [CrossRef]
13. Yang, Z.; Huang, B.; Kang, A.; Zhu, B.; Han, J.; Yin, R.; Li, X. Experimental study on the solitary wave-current interaction and the combined forces on a vertical cylinder. *Ocean. Eng.* **2021**, *236*, 109569. [CrossRef]
14. Zang, Z.; Chen, Z.; Zhao, M.; Xu, W.; Chen, Y. Experimental study on dynamic responses of a tensioned flexible vertical cylinder under waves and combined current and waves. *Ocean. Eng.* **2022**, *266*, 113159. [CrossRef]
15. Xin, Z.; Li, X.; Li, Y. Coupled effects of wave and depth-dependent current interaction on loads on a bottom-fixed vertical slender cylinder. *Coast. Eng.* **2023**, *183*, 104304. [CrossRef]
16. Huo, S.; Deng, S.; Song, Z.; Zhao, W.; Wan, D. On the hydrodynamic response and slamming impact of a cylindrical FPSO in combined wave-current flows. *Ocean. Eng.* **2023**, *275*, 114139. [CrossRef]
17. Ning, D.; Lin, H.; Teng, B.; Zou, Q. Higher harmonics induced by waves propagating over a submerged obstacle in the presence of uniform current. *China Ocean. Eng.* **2014**, *28*, 725–738. [CrossRef]
18. Saincher, S.; Sriram, V.; Agarwal, S.; Schlurmann, T. Experimental investigation of hydrodynamic loading induced by regular, steep non-breaking and breaking focused waves on a fixed and moving cylinder. *Eur. J. Mech. -B/Fluids* **2022**, *93*, 42–64. [CrossRef]

19. Zhou, X.; Jiang, Q.; Wang, Y.; Chen, L.; Wang, S.; Wang, K. Numerical Simulation of Wave–Current Force Characteristics of Horizontal Floating Cylinder in Heave Motion. *J. Mar. Sci. Eng.* **2022**, *10*, 1884. [CrossRef]
20. Belloli, M.; Giappino, S.; Morganti, S.; Muggiasca, S.; Zasso, A. Vortex induced vibrations at high Reynolds numbers on circular cylinders. *Ocean. Eng.* **2015**, *94*, 140–154. [CrossRef]
21. Dhanwani, M.A.; Sarkar, A.; Patnaik, B.S.V. Lumped parameter models of vortex induced vibration with application to the design of aquatic energy harvester. *J. Fluids Struct.* **2013**, *43*, 302–324. [CrossRef]
22. Sirohi, J.; Mahadik, R. Harvesting wind energy using a galloping piezoelectric beam. *J. Vib. Acoust.* **2012**, *134*, 11009. [CrossRef]
23. Abdelkefi, A.; Yan, Z.; Hajj, M.R. Modeling and nonlinear analysis of piezoelectric energy harvesting from transverse galloping. *Smart Mater. Struct.* **2013**, *22*, 025016. [CrossRef]
24. Bai, J.; Ma, N.; Gu, X. Wave-current loads on the horizontal cylinder with varying submergence depths. *J. Shanghai Jiao Tong Univ.* **2018**, *52*, 938–945.
25. Banaszek, A.; Petrovic, R.; Zyliński, B. FEM analysis of pipe material temperature changes influence on line expansion loops in hydraulic installations on modern tankers. *Therm. Sci.* **2011**, *15*, 81–90. [CrossRef]